

Spacetime Measurements with the Photon Ring

Rahul Kumar Walia,^{1,*} Prashant Kocherlakota,^{2,3} Dominic Chang,^{4,2} and Kiana Salehi^{5,6,7}

¹*Department of Physics, University of Arizona, 1118 E 4th Street, 85721 Tucson, USA*

²*Black Hole Initiative at Harvard University, 20 Garden St., Cambridge, MA 02138, USA*

³*Center for Astrophysics, Harvard & Smithsonian, 60 Garden St., Cambridge, MA 02138, USA*

⁴*Department of Physics, Harvard University, Cambridge, Massachusetts 02138, USA*

⁵*Perimeter Institute for Theoretical Physics, 31 Caroline Street North, Waterloo, ON, N2L 2Y5, Canada*

⁶*Department of Physics and Astronomy, University of Waterloo,*

200 University Avenue West, Waterloo, ON, N2L 3G1, Canada

⁷*Waterloo Centre for Astrophysics, University of Waterloo, Waterloo, ON N2L 3G1 Canada*

We explore the universal symmetries of the black hole photon ring in a wide range of non-Kerr spacetimes, including the Kerr-Newman, Kerr-Sen, Kerr-Bardeen, and Kerr-Hayward metrics. The demagnification exponent (γ) controls the size and flux scaling of higher-order images, which appear in the photon ring, the delay time (τ) determines the timing of their appearance, and the rotation parameter (δ) relates their relative orientations on the image plane. Our investigation reveals distinct responses of these critical parameters to black hole spin, generalized charge, and observer inclination: γ is predominantly influenced by charge and spin, τ is strongly affected by inclination, especially for near-extremal black holes, and δ is highly sensitive to spin. Notably, we find that the time delay provides an independent constraint on shadow size for polar observers, while the rotation parameter facilitates metric-independent spin measurements. Specifically, for Kerr black holes, the total variation in γ , τ , and δ across all possible inclinations is $\lesssim 10\%$, $\lesssim 20\%$, and $\lesssim 60\%$, respectively. By contrast, the Kerr shadow size varies by only $\lesssim 8\%$.

I. INTRODUCTION

Black holes (BHs) provide a rare and powerful laboratory to probe both gravitational physics and astrophysics simultaneously. Horizon-scale observations in the electromagnetic spectrum have recently become possible with the Event Horizon Telescope (EHT). These high-resolution, millimeter-wavelength observations of the supermassive BHs in Messier 87 (M87*) and in the Milky Way (Sgr A*) produced the historic first images of BH “shadows”, and are transforming our understanding of their environments and of the curved spacetime near event horizons [1–3]. The EHT images consistently display a ring-shaped feature known as “emission ring”, whose diameter closely traces the “critical curve” of the BH shadow boundary [4–9]. Due to limited angular resolution, the EHT has not yet been able to measure the spins of these BHs – a fundamental property with significant implications for BH formation, growth, accretion dynamics, galaxy-scale jet formation and even evolution on galactic scales. This is further complicated by the weak dependence of the size of the BH shadow on spin and inclination, varying by only $\sim 8\%$ for Kerr BHs [10, 11].

General relativity (GR) predicts that the strong gravitational lensing of extended emission sources around BHs produces a direct image as well as higher-order images, with the latter collectively referred to as the “photon ring” [12–16]. The photon ring has not yet been resolved in the EHT images. For optically-thin emission, the photon ring comprises an infinite sequence of *subrings* – formed by photons that complete at least half of a polar or latitudinal orbit around the BH photon shell before reaching our sky. These subrings display a

self-similar structure, and are indexed by the number of polar turning points or half polar-orbits completed en route to the observer, converging exponentially to the critical curve [15, 16]. Because photons travel along null geodesics of spacetime, these subrings carry distinct imprints of the near-horizon BH geometry, making them a “sweet spot” for studying the gravitational physics of BHs: They probe the near-horizon region, the leading-order subring remains observable at beyond-Earth baselines despite high redshift, and, importantly, they are minimally affected by the complex astrophysical processes in the accretion disk and jet base.

Photon rings are consistently seen in 3D general relativistic magnetohydrodynamic simulations of hot accretion flows around Kerr BHs [15, 17–20] as well as around non-Kerr BHs [21, 22]. Building on current capabilities, upcoming missions such as the next-generation EHT (ngEHT) [23] and the Black Hole Explorer (BHEX) [24] aim not only to detect the leading-order photon subring in the images of M87* and Sgr A* but also to measure its size and shape (see, e.g., Refs. [24–28]). Detecting the photon ring would confirm a strong prediction of GR, while measuring its geometric features (diameter, width, and shape) and visibility domain features would provide a BH mass and spin measurement, and potentially any deviation from the Kerr geometry, independent of astrophysical assumptions.

Non-Kerr BHs, both in GR or modified theories of gravity, feature “deviation parameters” or “generalized charges” in addition to mass and spin. The observable effects of these deviation parameters are expected to manifest in the strong-field regime near the event horizon. The EHT measurements of the shadow sizes of M87* and Sgr A* have been widely utilized to place constraints on potential deviations from the Kerr metric [9, 11, 29–34]. However, relying on a single observable often results in a degeneracy between the measurements of spin and deviation parameters from the Kerr solution. A Kerr

* rahulkumar@arizona.edu

BH shadow of a given size can be very well explained by a non-Kerr BH with different spin and non-zero charge [35, 36].

The prospect of observing photon ring in the near future has sparked significant interest [14–17]. While photon rings for Kerr BHs are relatively well-understood in terms of their image structure, polarization, and Fourier visibility [15–19, 37–44], their morphology in non-Kerr spacetimes is not fully understood yet (see, however, Refs. [40, 45–48]). In this paper, we aim to advance our current understanding of photon rings by addressing some key questions: How does the structure of the photon ring vary across different BH spacetimes? Can detections of the photon ring lead to robust BH spin measurement? And, most importantly, can joint measurements of the shadow size and specific photon ring features provide stringent constraints on deviations from Kerr spacetime?

Building on Ref. [16], in our previous paper [49], we have described the three critical parameters (γ_p , τ_p , δ_p) that govern the demagnification, time delay, and rotation, respectively, of successive photon subrings on the image plane in a broad class of stationary and axisymmetric spacetimes. In Ref. [49], we employed the Johannsen-Psaltis (JP) metric [50] – a four-dimensional, geodesically-integrable, spinning metric – to determine the critical parameters in terms of two metric functions and the observer’s inclination angle.¹ This metric is widely adopted for studying strong-field effects in a theory-agnostic framework, as it can represent a broad range of non-Kerr BHs in GR and modified theories. To systematically investigate variations in photon ring morphology across different spinning spacetimes, we analyze specific BH solutions, including Kerr-Newman [52], Kerr-Sen [53], Kerr-Bardeen [54], and Kerr-Hayward [54]. These non-Kerr spacetimes are controlled by an additional “charge” parameter Q , arising from their underlying physical fields, in addition to the total mass M and spin a . All of these metrics reduce to the Kerr metric in the limit of vanishing charge. Through this analysis, we quantitatively assess the potential of photon ring measurements to constrain strong-field deviations from the Kerr geometry, with the following key outcomes:

1. The demagnification exponent γ_p is always smaller than its Schwarzschild BH value (π), implying that photon subrings in non-Kerr spacetimes are always wider and brighter than in a Schwarzschild BH spacetime.
2. The delay time τ_p provides an independent measurement of the BH shadow size for observers present close to its spin-axis (e.g., M87*).
3. The rotation parameter δ_p yields a robust metric-independent spin measurement.

Thus, higher-order images, i.e., photon subrings, serve as “fingerprints” of the spacetime geometry, as they are governed by three purely geometric critical parameters.

The paper is organized as follows: In Section II, we present a brief review of the definitions of the lensing critical parameters in this broad class of stationary and axisymmetric, integrable BH spacetimes. In Section III, we explore the variation of these critical parameters in various non-Kerr spacetimes, examining both the impact of deviation parameters and observer’s inclination angle. We discuss the implications for BH spin measurements and constraints on Kerr-deviation parameters that could be obtained from future photon ring observations. Finally, we summarize our findings in Section IV.

II. PHOTON RING CRITICAL PARAMETERS

The Johannsen-Psaltis (JP) metric in Boyer-Lindquist coordinates, $x^\mu = (t, r, \vartheta, \varphi)$, is expressed as [50, 51]

$$\begin{aligned} ds^2 = & -\frac{\Sigma}{\Pi^2}(N^2 - F^2 a^2 \sin^2 \vartheta) dt^2 \\ & - 2\frac{\Sigma}{\Pi^2}(rF - N^2)a \sin^2 \vartheta dt d\varphi \\ & + \frac{\Sigma}{\Pi^2}(r^2 - N^2 a^2 \sin^2 \vartheta) \sin^2 \vartheta d\varphi^2 \\ & + \frac{\Sigma B^2}{r^2 N^2} dr^2 + \Sigma d\vartheta^2, \end{aligned} \quad (1)$$

where

$$\Sigma(r, \vartheta) = r^2 + f(r) + a^2 \cos^2 \vartheta, \quad (2)$$

$$\Pi(r, \vartheta) = r - Fa^2 \sin^2 \vartheta. \quad (3)$$

The metric functions N , F , and f can be freely chosen to describe a large class of integrable spacetimes, not restricted to only BH spacetimes. The metric function B can be eliminated through a change of the radial coordinate, $d\rho = B(r)dr$.

The coordinate 4-velocity of an arbitrary photon, $k^\mu = dx^\mu/d\lambda_m$, where λ_m is the Mino time along its trajectory, is

$$k^\mu = (\mathcal{T}_r + a^2 \cos^2 \vartheta, \pm_r \sqrt{\mathcal{R}}, \pm_\vartheta \sqrt{\Theta}, \Phi_r + \xi \csc^2 \vartheta). \quad (4)$$

In the above, we have introduced the so-called null geodesic effective potentials² $\{\mathcal{T}_r(r), \mathcal{R}(r), \Theta(\vartheta), \Phi_r(r)\}$,

$$\begin{aligned} \mathcal{T}_r &= \frac{r}{N^2}(r - Fa\xi) + a\xi - a^2, \\ \mathcal{R} &= \frac{r^2}{B^2} [(r - Fa\xi)^2 - N^2 \mathcal{J}^2], \\ \Theta &= \mathcal{J}^2 - (\xi \csc \vartheta - a \sin \vartheta)^2, \\ \Phi_r &= \frac{aF}{N^2}(r - Fa\xi) - a, \end{aligned} \quad (5)$$

¹ The JP metric [50] is described by four independent metric functions f , F , N , B in general. However, we have shown in Sec. II of Ref. [51] that the metric function f can be absorbed into the “Mino time” and that the metric function B can be eliminated via a radial coordinate transformation. Thus, null geodesics in the JP metric and the critical lensing parameters are completely determined by F and N .

² This is inspired by equations of the form $\dot{r}^2 = \mathcal{R}$ or $\dot{\vartheta}^2 = \Theta$, which are akin to “energy equations.”

with E the conserved energy of the photon, $E\xi = L$ its conserved azimuthal angular momentum, and \mathcal{I} its dimensionless non-negative Carter constant. Adding a constant to the Carter constant yields another Carter constant, e.g.,

$$\eta = \mathcal{I}^2 - (\xi - a)^2. \quad (6)$$

Note, however, that shifting the Carter constant in this way does not change the photon orbit. Eqs. (4) and (5) reveal that knowledge of the metric functions N and F is sufficient to determine the orbits of arbitrary photons in a JP spacetime (we can set $B = 1$ through a change of r , as discussed above).

The conserved quantities (ξ, \mathcal{I}) can be used to understand image formation. If we set up Cartesian coordinates (α, β) to describe the image plane of a faraway observer located at an inclination $\vartheta = i$ relative to the BH spin axis ($\vartheta = 0$), then the location at which an arbitrary photon appears is given simply as [12],

$$\alpha = -\xi \csc i; \quad \beta = \pm_{\vartheta} \sqrt{\Theta(i)}, \quad (7)$$

where the sign \pm_{ϑ} corresponds to sign of the polar angular momentum k_{ϑ} at the location of the observer. Thus, the conserved quantities (ξ, \mathcal{I}) directly determine the impact parameters of the photon.

Strong gravitational lensing close to a BH can compel photons to move on bound spherical orbits. The radial velocity, $|\dot{r}| = \mathcal{R}$, and acceleration, $|\ddot{r}| = \partial_r \mathcal{R}/2$, of photons on such spherical null geodesics (SNGs) both must naturally vanish. This is sufficient to infer the impact parameters (ξ_p, \mathcal{I}_p) of an SNG on a sphere of radius $r = r_p$ as being

$$\xi_p = \frac{1}{a} \frac{N - r \partial_r N}{N \partial_r F - F \partial_r N} \Big|_{r_p}; \quad \mathcal{I}_p = - \frac{F - r \partial_r F}{N \partial_r F - F \partial_r N} \Big|_{r_p}. \quad (8)$$

The shape and, in particular, the radial extent of the photon shell is determined simply by demanding that the 4-velocities of the SNGs are real-valued. For this consideration, the polar angular velocity, $\dot{\vartheta}$, of SNGs alone plays a nontrivial role. Requiring that

$$\Theta(\vartheta) \geq 0, \quad (9)$$

determines the shape of the photon shell in a BH spacetime.

The equality in Eq. (9) locates the outermost $r = r_p^+$ and innermost $r = r_p^-$ bound null orbits in the BH exterior. These are the retrograde ($\xi_p < 0$) and the prograde ($\xi_p > a$) equatorial circular photon orbits respectively. These radii r_p^{\pm} respectively are the largest roots of the two equations

$$\mp a(F - r \partial_r F) + (N - r \partial_r N) - a^2(N \partial_r F - F \partial_r N) = 0. \quad (10)$$

Within the photon shell, there is only one SNG of radius $r = r_p^0$ that reaches the poles and is a zero angular momentum orbit, $\xi_p^0 = 0$. The outer photon shell $r_p^0 < r \leq r_p^+$ permits only retrograde SNGs whereas its inner region $r_p^- \leq r < r_p^0$ permits only prograde ones.

The polar motion of an arbitrary SNG corresponds to oscillations between its two polar turning points $\vartheta = \vartheta_{\pm}$, which are, once again, obtained from the equality in Eq. (9), i.e.,

$\Theta(\vartheta_{\pm}) = 0$. In terms of $u = \cos^2 \vartheta$, this equation reduces to a simple quadratic equation in u [16],

$$(1 - u)\Theta(u) = \eta - a^2u^2 + (a^2 - \eta - \xi^2)u = 0, \quad (11)$$

the solutions to which are given as

$$u_{\pm} = \Delta_{\vartheta} \pm \sqrt{\Delta_{\vartheta}^2 + \frac{\eta}{a^2}}; \quad \Delta_{\vartheta} = \frac{1}{2} \left[1 - \frac{\eta + \xi^2}{a^2} \right]. \quad (12)$$

Since SNGs have non-negative η ($= \Theta(\pi/2)$), we can see that only $u_+ > 0$ for such orbits. Their polar turning points ϑ_{\pm} are then given as,

$$\vartheta_{\pm} = \arccos(\mp \sqrt{u_+}). \quad (13)$$

In addition to the solutions in Eq. (12), the polar turning point in Eq. (11) also has a trivial solution $u = 1$, satisfied by zero angular momentum orbits (ZAMOs, $\xi_p^0 = 0$). ZAMOs have trivial polar turning points corresponding to the poles of the coordinate system, $\vartheta = 0, \pi$. The ZAMO SNG, in particular, is located, as noted above, at $r = r_p^0$.

With the above, we are now in a position to introduce the lensing critical parameters. These are given as [49]

$$\begin{aligned} \gamma_p &= \sqrt{\frac{\partial_r^2 \mathcal{R}_p}{2}} \hat{G}_{\vartheta}, \\ \tau_p &= \left[\frac{r_p}{N_p} \mathcal{I}_p + a \xi_p - a^2 \right] \hat{G}_{\vartheta} + a^2 \hat{G}_t, \\ \delta_p &= a \left[\frac{F_p}{N_p} \mathcal{I}_p - 1 \right] \hat{G}_{\vartheta} + \xi_p \hat{G}_{\varphi} + 2\pi H(r - r_p^0), \end{aligned} \quad (14)$$

where, in the above, $H(x)$ is the Heaviside step function. These critical parameters not only govern the nearly-bound photon orbits around the BH but also determine the scaling of higher-order subrings on the image screen. We have also introduced the hatted functions \hat{G} which are given in terms of complete elliptic functions as follows [16, 55]

$$\begin{aligned} \hat{G}_{\vartheta} &:= \int_{\vartheta_-}^{\vartheta_+} \frac{1}{\sqrt{\Theta(\vartheta)}} d\vartheta = \frac{2}{a\sqrt{-u_-}} K\left(\frac{u_+}{u_-}\right), \\ \hat{G}_t &:= \int_{\vartheta_-}^{\vartheta_+} \frac{\cos^2 \vartheta}{\sqrt{\Theta(\vartheta)}} d\vartheta = -\frac{4u_+}{a\sqrt{-u_-}} E'\left(\frac{u_+}{u_-}\right), \\ \hat{G}_{\varphi} &:= \int_{\vartheta_-}^{\vartheta_+} \frac{\csc^2 \vartheta}{\sqrt{\Theta(\vartheta)}} d\vartheta = \frac{2}{a\sqrt{-u_-}} \Pi\left(u_+ \middle| \frac{u_+}{u_-}\right), \end{aligned} \quad (15)$$

with $K(k)$ the complete elliptic function of the first kind, $E'(k)$ the derivative of the complete elliptic function of the second kind w.r.t. the elliptic modulus k , i.e., $E'(k) := [E(k) - K(k)]/(2k)$, and $\Pi(n|k)$ the complete elliptic integral of the third kind, with n denoting the elliptic characteristic. Our convention for the elliptic functions can be found in Ref. [49].

The prefactor of the term involving \hat{G}_{ϑ} in γ_p is the (Mino time) phase space Lyapunov exponent, $\kappa_p = (\partial_r^2 \mathcal{R}_p/2)^{1/2}$. This Lyapunov exponent measures the radial instability of the

SNGs, and governs the radial deviation, $\delta r(\lambda_m)$, of nearly-bound photon orbits from their bound counterparts (i.e., those having the same impact parameters),

$$\log \left[\frac{\delta r(\lambda_m)}{\delta r(0)} \right] \approx \pm \kappa_p \lambda_m \quad \text{or} \quad \delta r(\lambda_m) = \delta r(0) e^{\pm \kappa_p \lambda_m}. \quad (16)$$

In the above, $\delta r(0)$ represents the initial radial coordinate distance between the two orbits. For photons on radially-perturbed orbits that are moving away from (towards) the SNG, one picks the positive (negative) sign in the equations above.

The prefactors in the terms involving \hat{G}_θ in τ_p and δ_p are simply the values of the effective potentials \mathcal{T}_r and Φ_r (5) evaluated at $r = r_p$ respectively.

We have thus far described the critical parameters associated with an arbitrary SNG in the photon shell. The observer's inclination angle, i (i.e., the observer is located at $\vartheta = i$), constrains the portion of the photon shell, $\Theta(i) \geq 0$, that contributes to image formation. Essentially, photons with turning points whose interval does not include the observer's colatitude, i.e., $i \notin [\vartheta_-, \vartheta_+]$ can never reach the observer.

Furthermore, the nearly-bound null geodesics that do appear on the image plane appear at different image plane polar angles, ψ , where

$$\psi = \arctan(\beta/\alpha), \quad (17)$$

depending on their impact parameters (ξ_p, \mathcal{I}_p) . Thus, each of the lensing critical parameters is a function of ψ on the image plane of the observer.

In the following section, we will be interested in understanding the variation of the critical parameters with the observer's inclination. For this purpose, it will be useful to introduce the mean values of the critical parameters over the image plane polar angle as,

$$\begin{aligned} \langle \gamma \rangle_\psi &= \frac{1}{2\pi} \int_0^{2\pi} \gamma_p(\psi) d\psi, \\ \langle \tau \rangle_\psi &= \frac{1}{2\pi} \int_0^{2\pi} \tau_p(\psi) d\psi, \\ \langle \delta \rangle_\psi &= \left[\frac{1}{2\pi} \int_0^{2\pi} \delta_p(\psi) d\psi \right] \bmod 2\pi. \end{aligned} \quad (18)$$

It is worth noting here that the rotation parameter δ_p measures the image screen polar angle offsets between consecutive order images [16]. Therefore, it satisfies the following identity $\delta_p = \delta_p \bmod 2\pi$. For this reason, it can be useful to introduce a “wrapped” rotation parameter $\delta_{2\pi;p}$ as

$$\delta_{2\pi;p} = \delta_p \bmod 2\pi. \quad (19)$$

Below, however, we elect to *not* use the wrapped rotation parameter since when averaged, $\langle \delta_{2\pi;p} \rangle_\psi := (1/2\pi) \int_0^{2\pi} \delta_{2\pi;p}(\psi) d\psi$, it introduces unnecessary wrapping artifacts (see right column in Fig. 7). Instead, $\langle \delta \rangle_\psi$ defined in Eq. (18) above will describe the mean rotation parameter. The appendix A discusses this issue in further detail. We also address there the impact on our conclusions of our choice to use

the mean as a characteristic measure of the critical parameters on the image plane versus, e.g., the median. While the mean and median measurements of δ_p agree at small inclinations, they differ significantly at large inclinations, where, unlike the mean δ_p , the median δ_p remains nearly independent of inclination. This behavior can be partially attributed to the following reasoning: The portion of the photon shell contributing to the photon ring formation grows smoothly with the observer's inclination – ranging from a single SNG, r_p^0 , for a polar observer to the entire photon shell, $r_p^- \leq r < r_p^+$, for an equatorial observer. Thus, at large inclinations, different segments of the photon ring, constructed from distinct SNGs with varying BL radii, experience differential demagnification, delay, and rotation. While the mean, as a statistical average, is sensitive to outliers (extremely high or low values) caused by prograde and retrograde SNGs near the equatorial plane, the median is not. Therefore, the mean δ_p provides a more reliable statistical average than the median.

We further note that phase wrapping information is not readily available from snapshots of order- n and order- $(n+1)$ images. It is, however, possible to experimentally observe phase wrapping from *movies* of successive order images, by studying how the $n+1$ image changes under continuous motion of the n image. As an example, the phase wrapping associated with an orbiting hot spot could be found by marking images by their time stamps whenever they cross over the same screen angle ψ , and keeping note of whether they cross over in a clockwise or anticlockwise motion as the hot spot goes around one revolution. We refer the reader to Fig. 6 to illustrate how phase wrapping information affects δ_p .

Since we are simultaneously interested in understanding the variation of the critical parameters with spacetime geometry, we find it useful to work with the mean deviations of the critical parameters from their Schwarzschild BH values, for which they are constant along the photon ring and are expressed as [16],

$$\{\gamma, \tau, \delta\} = \{\pi, \sqrt{27}\pi M, \pi\}, \quad (20)$$

where M denotes the Arnowitt-Deser-Misner (ADM) mass of the spacetime. Throughout this work we assume that the ADM masses of all BH spacetimes considered here are precisely identical. In practice, this mass for both M87* and Sgr A* can be fixed via stellar-dynamics measurements [56, 57]. For BHs having the same ADM mass, we define the mean critical parameter deviations as

$$\langle \bar{\gamma} \rangle_\psi := \frac{\langle \gamma \rangle_\psi}{\pi} - 1; \quad \langle \bar{\tau} \rangle_\psi := \frac{\langle \tau \rangle_\psi}{\sqrt{27}\pi M} - 1; \quad \langle \bar{\delta} \rangle_\psi := \frac{\langle \delta \rangle_\psi}{\pi} - 1. \quad (21)$$

III. VARIATION OF CRITICAL PARAMETERS WITH OBSERVER INCLINATION AND NON-KERR SPACETIMES

In this section, we study the behavior of the critical parameters with varying spin, charge and observer inclination for a number of spinning BHs.

Though our calculations are specific to the limit of high image-order (large- n), we note that these results are indicative

of measurements that will become accessible from upcoming experiments such as the ngEHT and BHEX, which will resolve the $n = 1$ images of M87* and Sgr A*. Ref. [39] has recently analyzed the variation in the exact time delay between the appearance of the primary ($n = 0$) and secondary ($n = 1$) images of a point source in a Schwarzschild BH spacetime. While the theoretically predicted “critical” value of time delay in this spacetime is a constant ($\tau = \sqrt{27}\pi M$), the exact time delay depends linearly both on the radial location of the source as well as the relative inclination between source and observer. Nevertheless, for sources located roughly in the equatorial plane viewed from moderate inclinations, the difference between the exact time delay and the critical time delay is modest ($\lesssim 30\%$). We expect this trend to extend to the other critical parameters and to also be relevant to the spinning BH spacetimes considered in this work. Specifically, we anticipate that our large- n results will approximate the exact demagnification, time delay and rotation between the primary and secondary images of hotspots and accretion disks in images of M87* and likely also Sgr A*.

The Kerr, Kerr-Newman, and Kerr-Sen BH spacetimes contain curvature singularities in their interiors, whereas the Kerr-Bardeen and Kerr-Hayward BH spacetimes are regular everywhere. Furthermore, barring the Kerr solution, the remaining spacetimes contain self-gravitating matter. The Kerr-Newman spacetime [52] includes an electromagnetic field, the Kerr-Sen spacetime [53] contains a scalar field, an electromagnetic field, and an axion field, and regular BHs [54] involve exotic matter that violates classical energy conditions deep within their event horizons. In addition to spin (a), these BHs also carry a “generalized charge” (Q) due to their nontrivial matter content.

All of these BH models belong to the metric family described by Eq. (1), and are thus axisymmetric with integrable geodesic structure. Axisymmetry specifically implies that polar observers (present along the BH spin axis) will find no variations in the critical parameters when moving along the critical curve [37, 49]. Inclined observers will, however, witness a variation of the critical parameters that depends on the screen angle, ψ . The critical parameters are therefore usually functions of ψ for general observer inclinations.

Future observations, capable of resolving photon subrings, would be able to sample the critical parameters at multiple screen angles. For instance, resolved images of flares caused by orbiting hotspots might enable measurements of all three critical parameters by correlating intensity fluctuations across successive ordered images [41]. In practice, observables would likely be derived from averages of events across multiple occurrences of various phenomena.

Roughly motivated by these expectations, we study the variations in the ψ -averaged values of the critical parameters from their Schwarzschild values with varying spacetime geometries and observer inclinations. We discuss the impact of using the ψ -median values of the critical parameters as an alternative characteristic measure in Appendix B. The specific quantities we study are defined in Eq. (18) and Eq. (21). We represent our results through four main studies depicted in Figures 1, 2, 3 and 4 below.

Fig. 1 shows the variation in the mean values of the critical parameters in various spacetimes over varying observer inclination. More precisely, we present the fractional deviation of the mean values from their corresponding values in a Schwarzschild BH spacetime to highlight the impact of a nonzero BH spin and charge. To begin with, in this figure, we fix the spin and charge of the different BHs to intermediate values of $a = 0.5M$ and $Q = 0.4M$, respectively. The variation in all three critical parameters across the various spacetimes – containing a variety of matter fields – is modest ($\lesssim 5\%$) for all observer inclinations. For $a = 0.5M$ and $Q = 0.4M$, the demagnification exponent, the delay time, and the rotation parameter differ from their corresponding Schwarzschild values (20) by $\lesssim 10\%$, $\lesssim 5\%$, and $\lesssim 25\%$ respectively. This suggests that the demagnification exponent and the rotation parameter are more sensitive probes of the spacetime geometry than the delay time, independently of the observer’s inclination.

To better understand which aspects of the spacetime each critical parameter is sensitive to, we allow the BH spin to vary in Fig. 2. Since Fig. 1 indicated that the critical parameters are sensitive to the BH spin and charge but not the “details” of the spacetime geometry, we display our analysis for three representative spacetimes: Kerr BHs, Kerr-Newman BHs, and regular Kerr-Bardeen BHs. The BH charge is kept fixed to the previous value of $Q = 0.4M$. Thus, in this figure, the vertical red lines correspond to the BH models considered in Fig. 1.

Across the three different spacetimes, the mean time delay, $\langle\tau\rangle_\psi$, shown in the middle column, features complicated behaviour with varying BH spin and observer inclination. Nevertheless, it remains within $\approx 5\%$ of its Schwarzschild value, barring in the upper right quadrants. The sharp increase in the time delay at large spins and high inclinations can be seen as a consequence of the contributions from photon trajectories that approach within close vicinity of the BH event horizon. For an extremal ($a = M$) Kerr BH in particular, Eq. (13) can be used to show that photons with trajectories close to the horizon also remain close to the equatorial plane, and are, thus, only seen by observers located close to the equatorial plane. Finally, for typical (non-extremal) BHs, the delay time is fairly insensitive to the observer inclination.

In contrast to the delay time, the demagnification exponent (left column) and the rotation parameter (right column) have simpler behavior. The demagnification exponent is smaller and lies within about 20% of, its Schwarzschild value in all of these BH spacetimes. A smaller demagnification exponent indicates that photon subrings in these non-Kerr spacetimes will have larger widths and fluxes as compared to those in Schwarzschild BH spacetime.

The rotation parameter, on the other hand, is always found to be larger than its Schwarzschild value and is effectively insensitive to the observer’s inclination for moderate BH spin. This was expected from the spin-induced frame-dragging contribution in the rotation parameter for non-Kerr BHs. Furthermore, comparing isocontours of the same rotation parameter value across the different BH spacetimes shows that they appear at the same BH spin values. Combining these two observations indicate that the rotation parameter may be an excellent proxy for BH spin, independently of the observer inclination and the

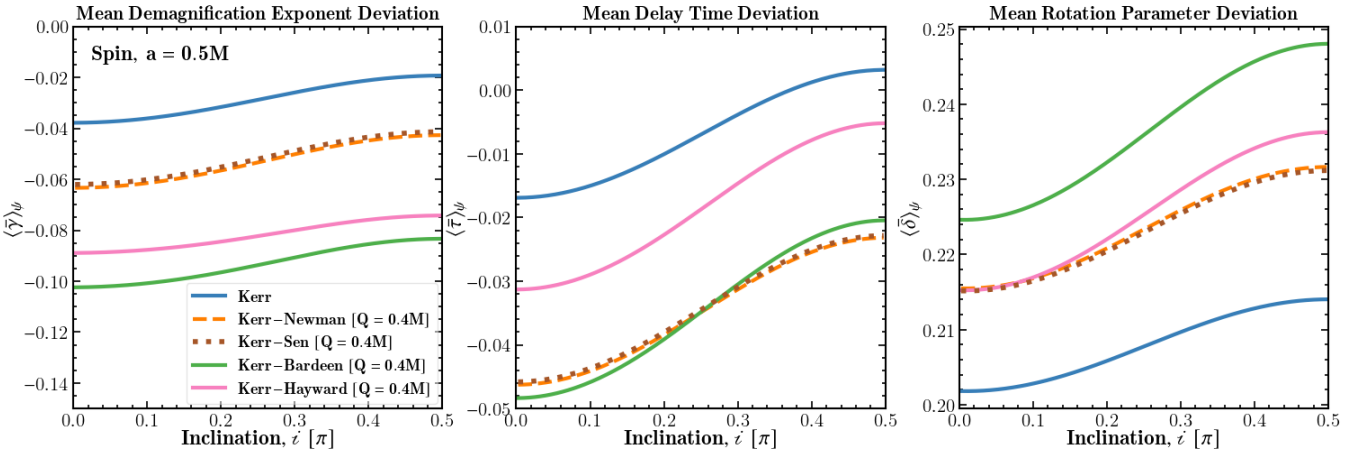


FIG. 1. Deviations of the mean demagnification exponent (left panel), time delay (center panel), and rotation parameter (right panel) of the Kerr, Kerr-Newman, Kerr-Sen, Kerr-Bardeen and Kerr-Hayward BHs from their Schwarzschild values, for varying observer inclinations. The spin, a , of each BH is fixed to $0.5M$ and the “generalized charge,” Q , of the non-Kerr BHs is set to $0.4M$. We find modest variations ($\lesssim 5\%$) in all three critical parameters across the different spacetimes, indicating that the critical parameters are sensitive to spin and charge.

specifics of the spacetime geometry.

To investigate whether the rotation parameter is truly a measure of the BH spin alone, we finally allow the BH charge of Kerr-Newman BH to vary in Fig. 3. As a reminder, the zero charge limit of the Kerr-Newman spacetime yields the Kerr spacetime. We show the mean rotation parameter in the right column as seen by an observer close to the BH spin axis at an inclination of 17° (top row) or located close to the equatorial plane ($i = 89^\circ$; bottom row). The former inclination was chosen to be consistent with the large scale jet of M87* [58], and the latter was chosen to be exemplary of cases with extremely high inclinations. These panels provide further evidence that the rotation parameter is typically an excellent measure of the BH spin, since the isocontours lines appear to be nearly parallel to the charge axis. Close to the extremal limit (circular red line), however, the rotation parameter does become sensitive to the BH charge.

We understand the sensitivity of the rotation parameter on the spin alone as a manifestation of the former measuring the magnitude of frame-dragging or gravitomagnetism experienced by nearly-bound photon orbits.

Furthermore, if such measurement yields a nonzero value in particular, it would correspond to a measurement of frame-dragging close to a BH horizon, directly analogous to a measurement of the gravitomagnetic precession of the Gravity Probe B gyroscopes in the Earth’s gravitational field or that measured in the double pulsar system [59].

The demagnification exponent (left column) shows almost equal sensitivity to both BH spin and charge, for this BH spacetime.

Finally, the delay time shows smooth variations with spin and charge at small inclinations (top middle panel). It appears to be relatively more sensitive to the BH charge, and remains within about $\lesssim 20\%$ of the Schwarzschild value. At large inclinations (bottom middle panel), the contribution of the nearly-equatorial photon orbits which, in near-extremal BHs,

approach the BH horizon, is clear to see.

In Fig. 4 we collect all of our insights from above into a prediction for future experimental measurements of spacetime geometry with high-resolution images of M87*. We overlay isocontours of the mean values of all the critical parameters of a Kerr-Newman BH, for an observer located at an inclination of 17° . Here, we additionally show the fractional deviation of the mean shadow size, $\langle \bar{\rho} \rangle_\psi$ of a Kerr-Newman BH from its Schwarzschild value ($\sqrt{27}M$) in blue isocontours as well as in the background color. In each case, the isocontours show 5% (solid), 10% (dashed), 20% (dot-dashed) and 25% (dotted) deviations from their Schwarzschild values. The white-shaded region here shows the constraints on Kerr-Newman BH parameter space from the 2017 EHT shadow size measurement of M87*, as described in Refs. [11, 30]. These indicative constraints were obtained by determining the deviation in the mass inferred from the emission ring in the image of M87* by the EHT [29], compared to that from stellar dynamics measurements [56].

It is clear from this figure that the isocontours of the shadow size and the delay time virtually lie on top of each other. Thus, the mean delay time provides an independent measure of the shadow size, at least for low observer inclinations. Furthermore, this figure illustrates the power of combining multiple measurements of the photon ring critical parameters to pin down physical properties of astrophysical BHs, *viz.*, their spin and charge.

Finally, to investigate whether the delay time always produces a robust measure of the shadow size, in Fig. 5, we replicate Fig. 4 but change the observer inclination to $i = 89^\circ$. It is immediately evident that both quantities, $\langle \bar{\gamma} \rangle_\psi$ and $\langle \bar{\rho} \rangle_\psi$, have distinct behaviors with varying BH spin and charge, and that they conspire to produce identical variations only for observers present on the BH spin axis. We have discussed this latter feature in Ref. [49] (see Eq. (44) there).

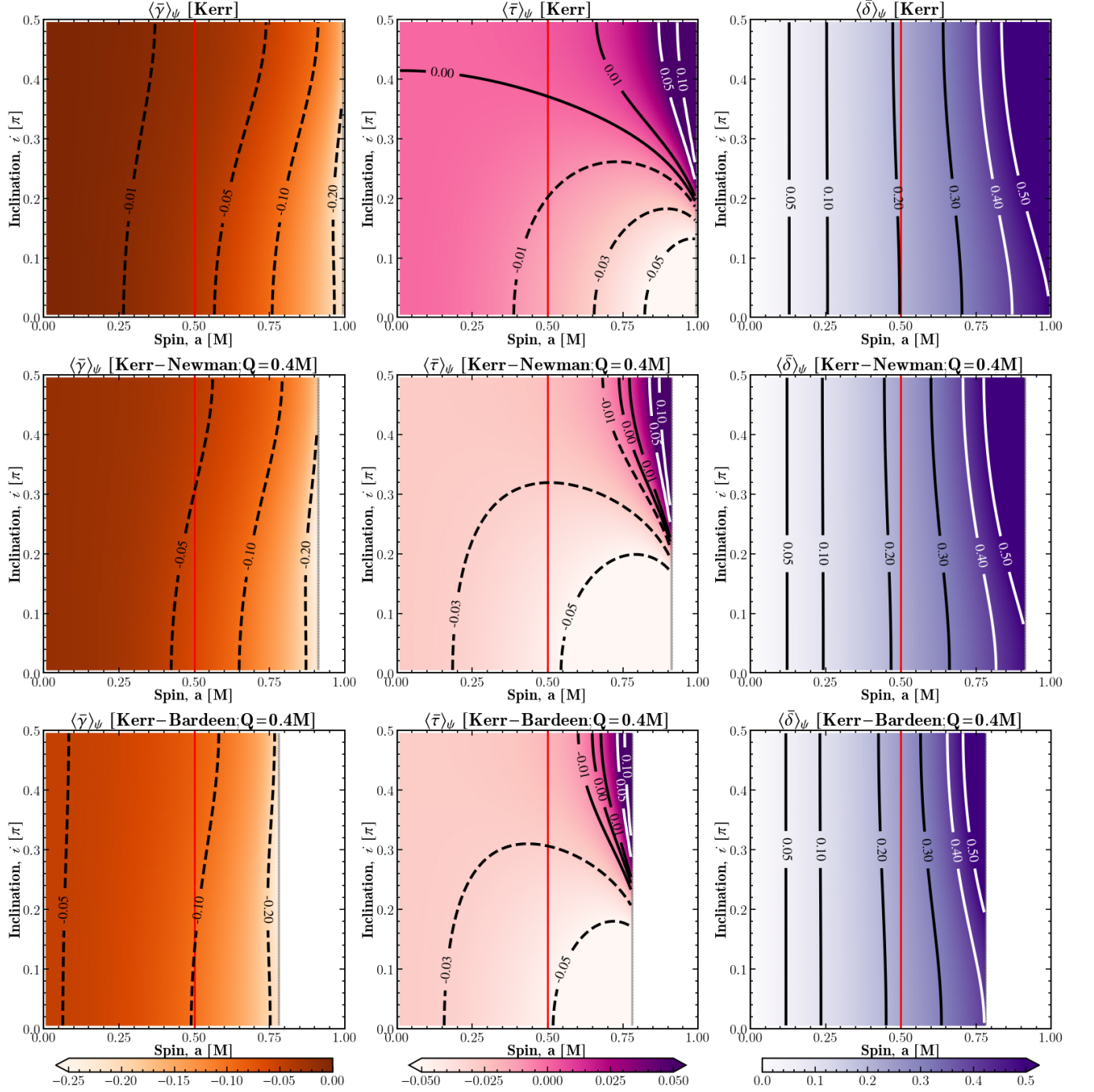


FIG. 2. Deviation of the (mean) critical parameters of the Kerr (top row), Kerr-Newman (middle row) and Kerr-Bardeen (bottom row) spacetimes from their Schwarzschild values, as a function of BH spin and observer inclination. The charge of the non-Kerr BHs is set to a middling value of $0.4M$, as in Fig. 1. The demagnification exponent (left column) is always smaller than its Schwarzschild value; Thus, secondary images are larger in non-Schwarzschild spacetimes. The time delay (middle column) increases sharply for an extremal BH viewed by an equatorial observer, due to the influence of photons orbiting extremely close to the event horizon. The rotation parameter (right column) is an excellent measure of BH spin, due to its insensitivity to observer inclination and specifics of the BH spacetime geometry.

IV. SUMMARY & CONCLUSIONS

Horizon-scale images of BHs have opened up a new avenue to probe strong-field gravity as well as specific properties of

astrophysical BHs, such as their spin. Of particular interest to future BH imaging observations, performed at higher angular-resolutions and flux-sensitivity, is the direct detection of the BH photon ring. Due to strong gravitational lensing, a single

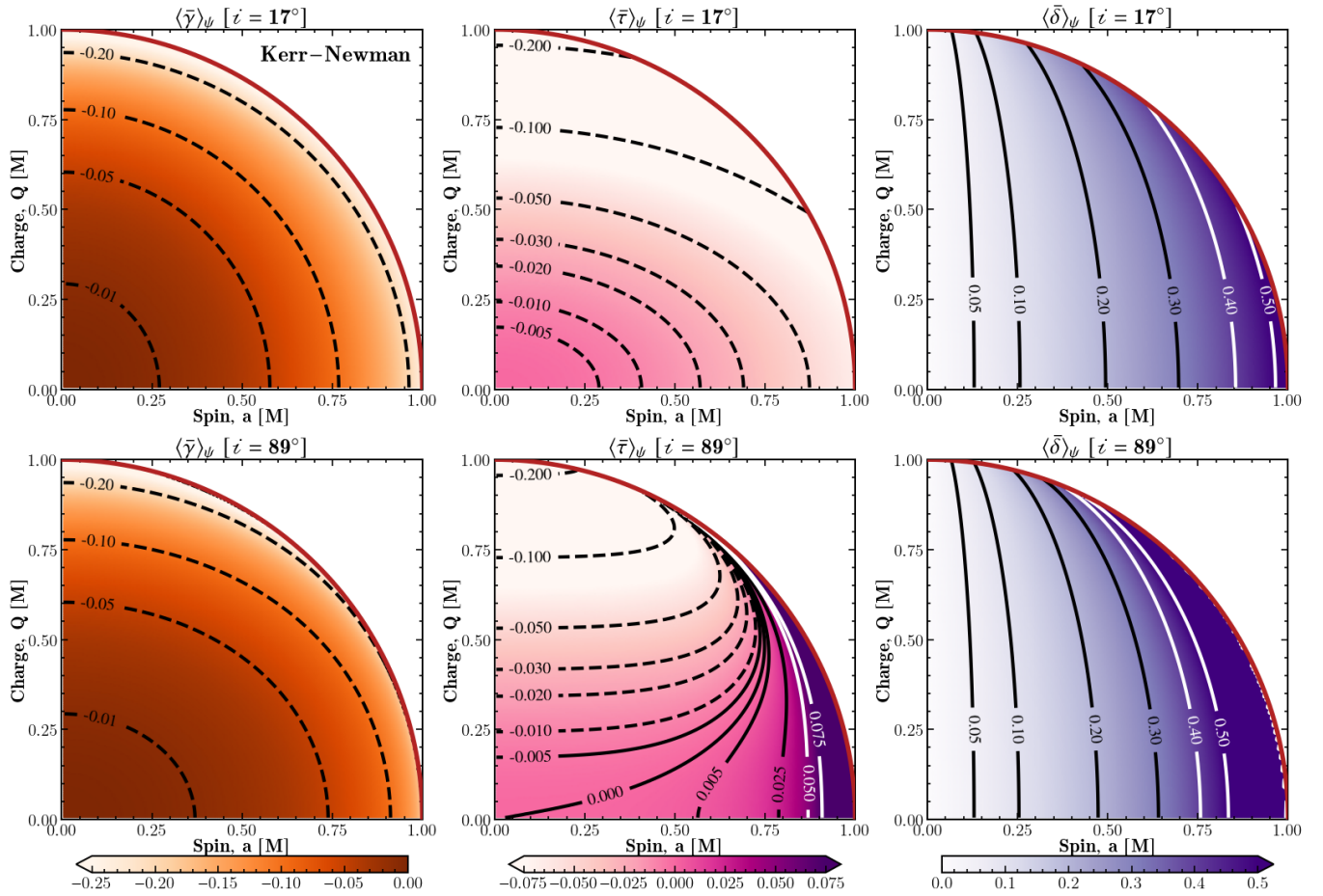


FIG. 3. Variation of the mean critical parameters of the Kerr-Newman spacetimes with charge and spin, as seen by an observer at a low inclination of 17° (top row) and high inclination of 89° (bottom row). Shown are the variations of fraction deviation of mean demagnification exponent ($\langle \bar{\gamma} \rangle_\psi$), the mean time delay ($\langle \bar{\tau} \rangle_\psi$) and the mean rotation parameter from their corresponding Schwarzschild BH values on the observer's screen (right column).

point source can create multiple images on the screen of an observer. The primary image is the first to arrive on the screen, whereas “higher-order” images appear at later times. Essentially, increasingly higher-order images are created by photons that execute multiple (half-)orbits around the BH. Thus, they carry unique signatures of the near-horizon spacetime geometry.

Our investigation here focuses on three critical parameters that characterize the universal relations between higher-order images: the demagnification exponent (γ), governs the demagnification of successive order images, the time delay (τ) determines the time elapsed between their appearance, and the rotation parameter (δ) relates their angular positions on the image plane. We present a comprehensive analysis of how these parameters vary across a diverse family of non-Kerr spacetimes — including the Kerr-Newman, Kerr-Sen, Kerr-Bardeen, and Kerr-Hayward metrics — as functions of BH spin (a), generalized charge (Q), and the observer’s inclination (i). In particular, we describe the fractional deviations of the azimuthally-averaged values of the critical parameters from their Schwarzschild BH values. We summarize our key

findings below.

The critical parameters respond distinctively to variations in a , Q , and i , establishing them as complementary probes of spacetime geometry. Specifically, the demagnification exponent is always smaller in non-Schwarzschild spacetimes (including Kerr) as compared to the Schwarzschild spacetime. This indicates that for primary images of the same size, the secondary images are always larger in non-Schwarzschild spacetimes. For polar observers, the delay time is an excellent proxy for the BH shadow size. Finally, the rotation parameter is an excellent measure of the BH spin, and is essentially insensitive to the BH charge, the specifics of the spacetime geometry (e.g., a Kerr-Newman vs. a Kerr-Bardeen of the same charge), and the observer inclination. Thus $\langle \bar{\gamma} \rangle_\psi \leq 0$ and $\langle \bar{\delta} \rangle_\psi \geq 0$ imply that photon subrings in these non-Kerr spacetimes are wider, brighter, and more rotated than those of the Schwarzschild BH.

While both γ and δ are nearly independent of inclination, τ is somewhat sensitive to i . In particular, the delay time rises sharply for near-extremal BHs viewed at high-inclinations, due to contributions from nearly-bound orbits that approach the close vicinity of the event horizon.

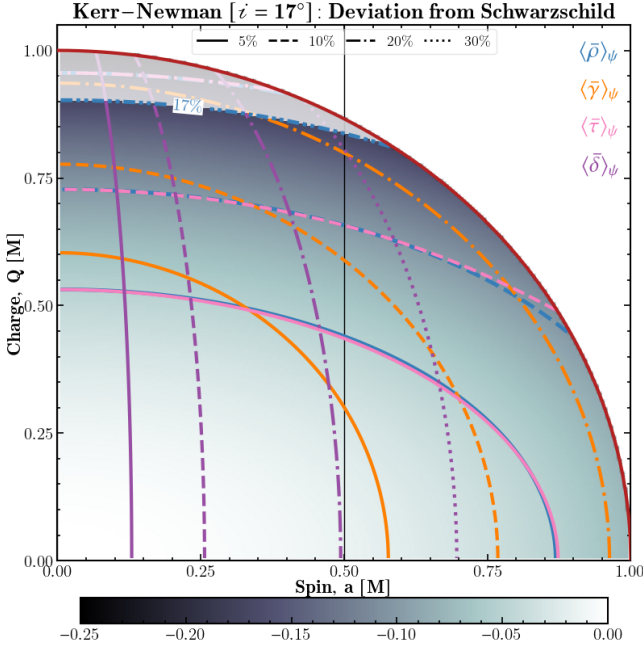


FIG. 4. Combining measurements of various critical parameters could pin down physical properties of astrophysical BHs. Shown here are the deviations in the shadow size (blue lines and background color), the demagnification exponent (orange), the time delay (pink), and the rotation parameter (purple) of a Kerr-Newman BH from their Schwarzschild values. The isocontours display 5% (solid), 10% (dashed), 20% (dot-dashed) and 30% (dotted) deviations. The white-shaded region is excluded by the 2017 EHT shadow size measurement of M87*. The isocontours of shadow size and delay time are virtually indistinguishable.

Quantitatively, for Kerr BHs, the fractional deviations across the full parameter space of spin and inclination are: $\sim 20\%$ in $\langle \bar{\gamma} \rangle_\psi$, $\sim 10\%$ in $\langle \bar{\tau} \rangle_\psi$, and $\sim 60\%$ in $\langle \bar{\delta} \rangle_\psi$ – significantly larger than the 8% variation in the shadow diameter.

A key finding of our analysis demonstrates that the time delay between successive photon rings serves as an independent measure of shadow size for nearly polar observer, even for spinning BHs. Our results establish that photon ring critical parameters can effectively constrain both BH spin and non-Kerr deviations. Using the Kerr-Newman metric as an example, we demonstrate that combining shadow size measurements with either the demagnification exponent or rotation parameter successfully breaks the degeneracy between spin and non-Kerr parameters.

While non-Kerr parameters provide a powerful framework for characterizing photon ring features, potential degeneracies between different spacetime solutions may limit their ability to uniquely identify the underlying spacetime geometry and deviations from the Kerr geometry.

ACKNOWLEDGMENTS

RKW's research is supported by the Fulbright-Nehru Postdoctoral Research Fellowship (Award No. 2847/FN-

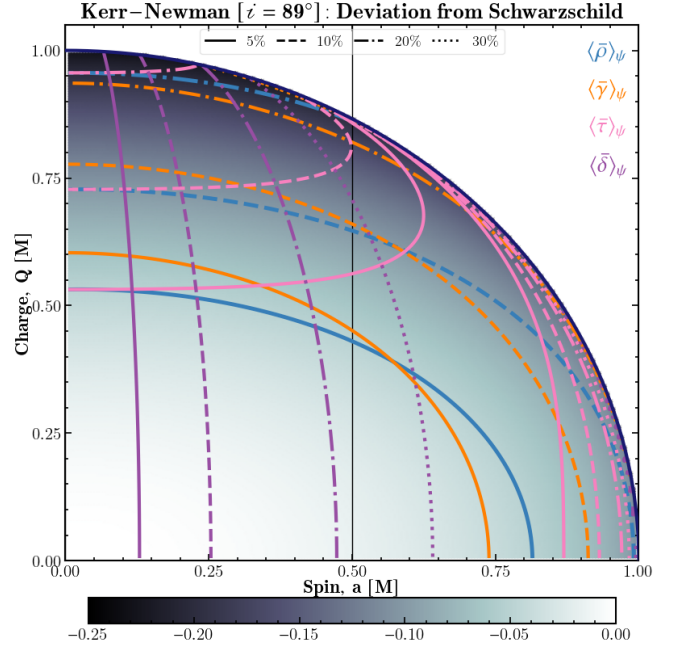


FIG. 5. Similar plot to Fig. 4 but for an observer present close to the equatorial plane. Notably, the delay time and the shadow size display distinct behaviors for Kerr-Newman BHs of different spin and charge for general observer inclinations. Nevertheless, the joint measurement of the shadow size and either of these critical parameters can precisely determine the BH spin and charge.

PDR/2022) from the United States-India Educational Foundation. PK acknowledges support from grants from the Gordon and Betty Moore Foundation (GBMF-8273) and the John Templeton Foundation (#62286) to the BH Initiative at Harvard University. The Perimeter Institute for Theoretical Physics partially supported this work. Funding for research at the institute is provided by the Department of Innovation, Science and Economic Development Canada, and the Ministry of Economic Development, Job Creation and Trade of Ontario, both of which are branches of the Government of Canada.

Appendix A: Representative Measures of The critical Parameters

For spinning BHs, the observer's inclination angle, ι , determines the part of photon shell, $r_p^- \leq r \leq r_p^+$, satisfying $\Theta(\iota) \geq 0$, that contributes to the image formation on the observer's screen. This leads to a rich phenomenology where polar observers ($\iota = 0, \pi$) see perfectly circular photon subrings formed exclusively by photons on the polar SNG at radius r_p^0 , while equatorial observers access the complete photon shell, resulting in maximal image distortion, with smooth variation at intermediate inclinations. As the image plane polar coordinate ψ varies along a photon subring or the critical curve, we trace SNGs of different BL radii within the visible portion of the photon shell, transitioning from retrograde orbits at $\psi = 0$ to prograde orbits at $\psi = \pi$.

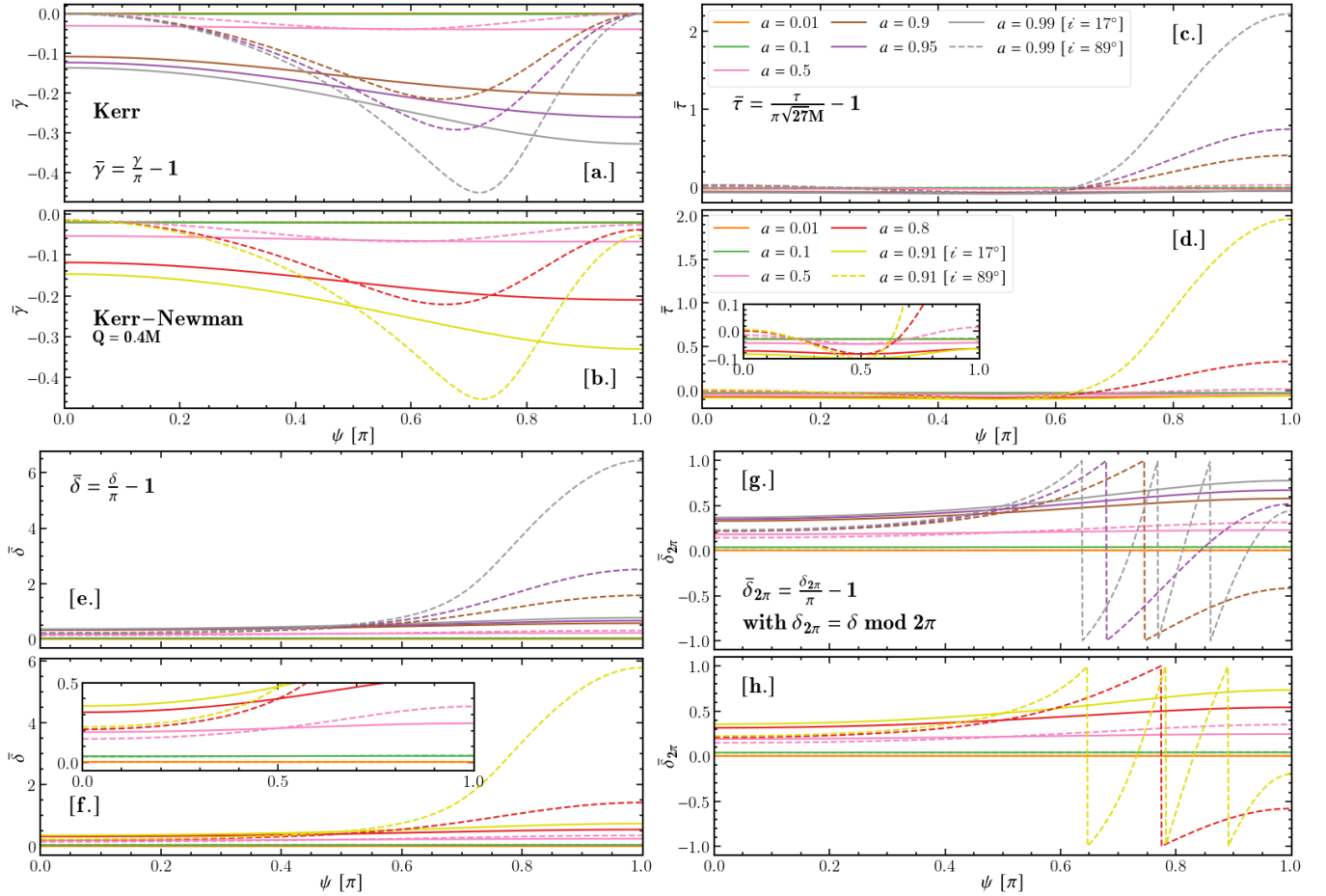


FIG. 6. Variation of fractional deviation in critical parameters for the Kerr (panels [a.], [c.], [e.], [g.]) and $Q = 0.4$ Kerr-Newman (panels [b.], [d.], [f.], [h.]) BHs. All deviations are shown with respect to their Schwarzschild values over varying image plane polar angle ψ . These are the Schwarzschild relative deviations of the demagnification exponent, \bar{y} , (panels [a.] and [b.]), the delay time between successive images, $\bar{\tau}$, ([c.] and [d.]), the rotation parameter, $\bar{\delta}$, ([e.] and [f.]), and the phase wrapped rotation parameter, $\bar{\delta}_{2\pi}$, ([g.] and [h.]). We show deviation curves for varying spin values varying from 0.01 to 99% of extremality for space times in varying colors, and for observer inclination angles of an M87*-like system of 17° (solid), and for an extreme inclination case of 89° (dashed). The insets of [d.] and [f.] displayed a zoomed in version of their encompassing panels.

These critical parameters (14), functions of SNG radius r_p , can be expressed in terms of ψ using Eq. (17). For polar inclination angles, these parameters remain constant along the photon ring. However, for non-polar inclinations ($i \neq 0, \pi$), they vary with ψ , causing distinct portions of the photon ring to be demagnified, rotated, and delayed by varying amounts (see Fig. 6).

Figure 6 shows the fractional deviation of critical parameters from their Schwarzschild values as a function of image plane polar angle ψ for both Kerr and Kerr-Newman BHs. We analyze these deviations at two distinct inclination angles (17° and 89°) across various spin parameters. The results demonstrate that critical parameters in spinning BHs exhibit ψ -dependent variations, with this effect becoming particularly pronounced at higher inclinations.

While $\bar{y} < 0$ for all values of a and i , at high inclinations, \bar{y} exhibits non-monotonic variation between $\psi = 0$ and $\psi = \pi$, reaching a minimum at an intermediate value. This minimum

in \bar{y} corresponds to the screen angle where the photon ring appears widest and brightest. Monotonically increasing time delay with ψ is an indicator that the distinct part of a given order photon ring takes distinct time to appear. This temporal variation arises because prograde photons $r_p \leq r_p^0$ forming a part of photon ring takes longer to reach the observer's screen compared to their retrograde counterparts.

For BHs with high spin parameters and large inclination angles, photon ring segments can experience rotations exceeding 2π radians, as demonstrated in the lower panel of Fig. 6 where the rotation parameter $\delta_p \geq 2\pi$. When imaging static sources, the measured rotation parameter $\delta_{p,2\pi}$ displays a zigzag pattern.

Time-resolved observations of dynamic emission sources around BHs could potentially reveal both temporal variations in photon ring formation and segments rotated beyond 2π . These phenomena present compelling targets for future time-domain observations of BH dynamics.

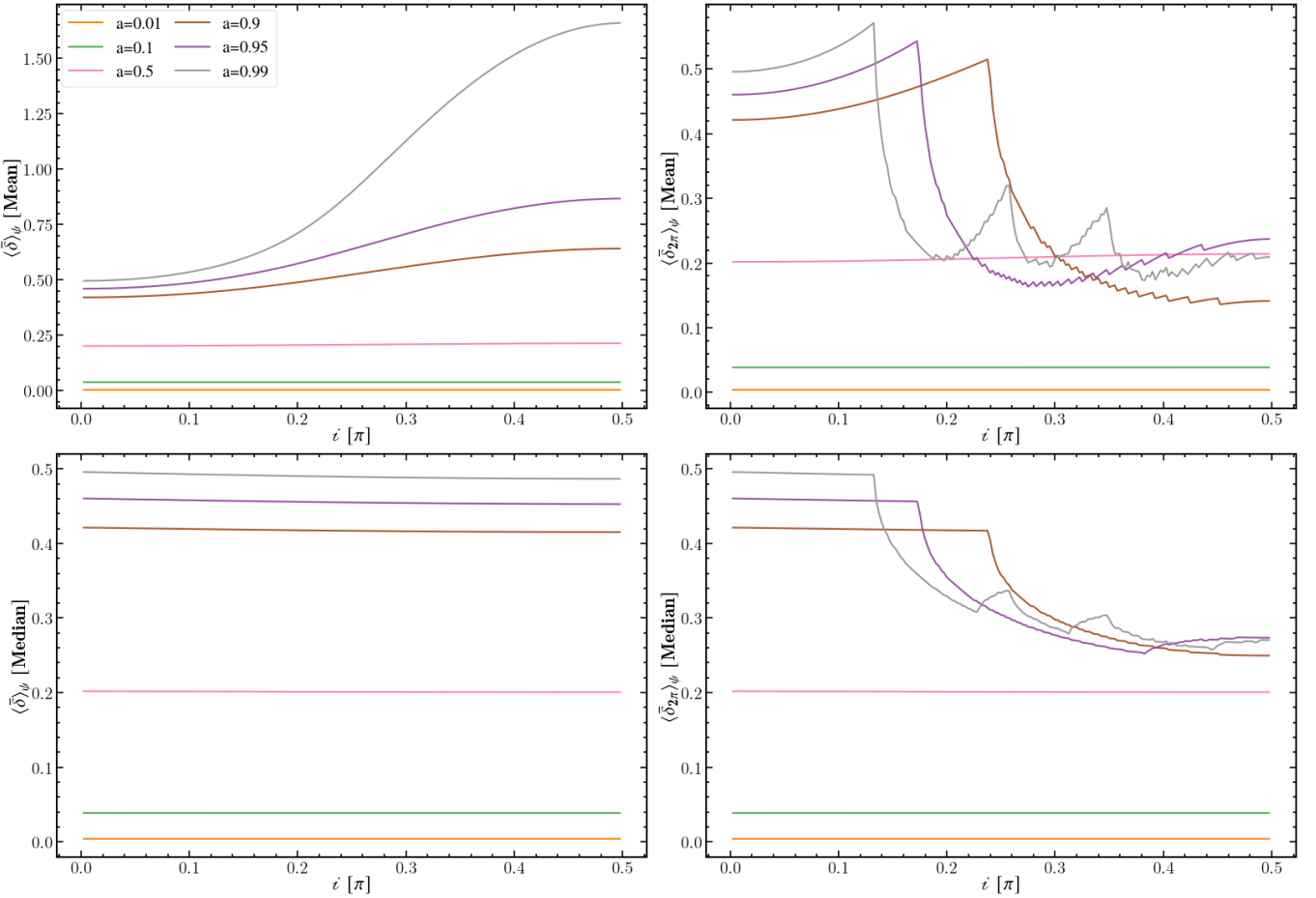


FIG. 7. Figure illustrating different statistical measures of the critical rotation parameter along the photon ring. We show the un-phase wrapped statistics in the left column, and the phased wrapped statistics in the right column, where we have applied a 2π modulo operation before constructing the statistics. We specifically show the screen averaged mean (top row) and median (bottom row) values. Whether the 2π modulo operation must be taken before the statistic is dependent on the nature of the underlying observation (See the discussion at the end of Sec. II). We adopt the mean value as our primary measure, although they vary more over observer inclination than their corresponding median values, especially at high values of inclinations. Unlike the median, which remains largely insensitive to inclination (see bottom-left sub-figure), the mean captures the inclination's imprint and varies smoothly with it. Additionally, averages having modulo operation after statistical averaging, exhibit smooth variations with inclination angle

For quantitative analysis, statistical measures of the critical parameter along the photon ring are required. We evaluated four distinct methods to determine the rotation parameter: (i) $\text{median}[\text{mod}(\delta, 2\pi)]$, (ii) $\text{mean}[\text{mod}(\delta, 2\pi)]$, (iii) $\text{mod}[\text{median}(\delta, 2\pi)]$, and (iv) $\text{mod}[\text{mean}(\delta, 2\pi)]$. Figure 7 presents these measurements for a Kerr BH as a function of spin with varying inclination. Methods (iii) and (iv), which apply the modulo operation after statistical averaging, exhibit smooth variations with inclination angle, while methods (i) and (ii) show multiple discontinuities, suggesting measurement artifacts. Based on these results, we adopt $\text{mod}[\text{mean}(\delta, 2\pi)]$ for our rotation parameter calculations.

Appendix B: Variation with Non-Kerr Parameter

Non-Kerr BHs considered in this paper are characterized by a charge parameter Q in addition to mass M and spin a . The influence of charge on BH shadow morphology has been extensively studied in both spherically symmetric and rotating spacetimes, with corresponding observational constraints [30].

Figure 8 illustrates the charge dependence of photon ring critical parameters across different spacetime geometries at observer's inclination of 17° and 89° . Our results demonstrate that charge induces distinct modifications to various critical parameters. Notably, for all BH solutions examined, we find $\langle \bar{\gamma} \rangle < 0$ and $\langle \bar{\delta} \rangle > 0$ across all charge values, with maximal effects manifesting in near-extremal configurations.

Among all observables studied, the demagnification exponent governing ring demagnification demonstrates maximum charge sensitivity, whereas rotational dynamics exhibits mini-

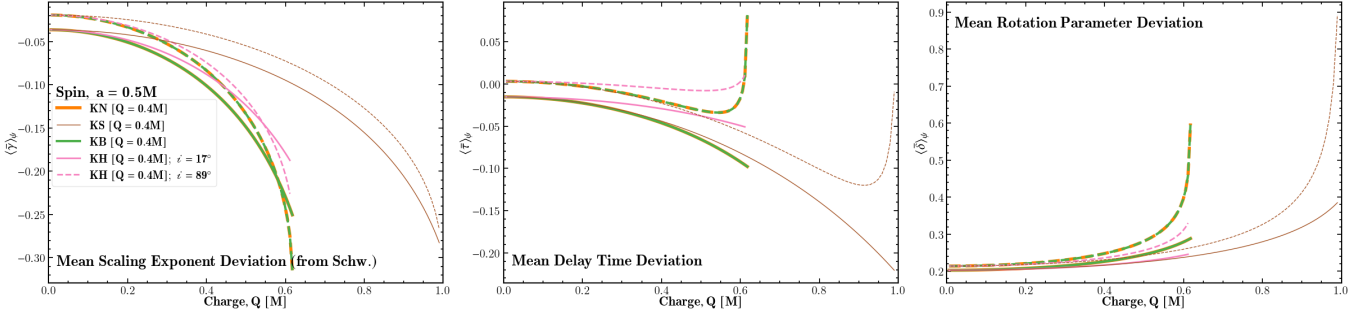


FIG. 8. Variation of critical parameters with charge in non-Kerr BHs. The fractional deviation of the mean values of the demagnification exponent and time delay from their Schwarzschild counterparts decreases and increases monotonically, respectively, with increasing charge. For non-extremal BHs, the time delay decreases with charge. However, for large inclinations and near-extremal BHs, it sharply increases due to photons traversing paths very close to the extremal horizon.

mal charge dependence.

[1] K. Akiyama *et al.* (Event Horizon Telescope), First M87 Event Horizon Telescope Results. I. The Shadow of the Supermassive Black Hole, *Astrophys. J. Lett.* **875**, L1 (2019), arXiv:1906.11238 [astro-ph.GA].

[2] K. Akiyama *et al.* (Event Horizon Telescope), First Sagittarius A* Event Horizon Telescope Results. I. The Shadow of the Supermassive Black Hole in the Center of the Milky Way, *Astrophys. J. Lett.* **930**, L12 (2022), arXiv:2311.08680 [astro-ph.HE].

[3] K. Akiyama *et al.* (Event Horizon Telescope), The persistent shadow of the supermassive black hole of M87. I. Observations, calibration, imaging, and analysis, *Astron. Astrophys.* **681**, A79 (2024).

[4] R. Narayan, M. D. Johnson, and C. F. Gammie, The Shadow of a Spherically Accreting Black Hole, *apjl* **885**, L33 (2019), arXiv:1910.02957 [astro-ph.HE].

[5] T. Bronzwaer *et al.*, Visibility of black hole shadows in low-luminosity AGN, *mnras* **501**, 4722 (2021), arXiv:2011.00069 [astro-ph.HE].

[6] P. Kocherlakota and L. Rezzolla, Distinguishing gravitational and emission physics in black hole imaging: spherical symmetry, *mnras* **513**, 1229 (2022), arXiv:2201.05641 [gr-qc].

[7] F. Özel, D. Psaltis, and Z. Younsi, Black Hole Images as Tests of General Relativity: Effects of Plasma Physics, *Astrophys. J.* **941**, 88 (2022), arXiv:2111.01123 [astro-ph.HE].

[8] Z. Younsi, D. Psaltis, and F. Özel, Black Hole Images as Tests of General Relativity: Effects of Spacetime Geometry, *Astrophys. J.* **942**, 47 (2023), arXiv:2111.01752 [astro-ph.HE].

[9] K. Akiyama *et al.* (Event Horizon Telescope), First Sagittarius A* Event Horizon Telescope Results. VI. Testing the Black Hole Metric, *Astrophys. J. Lett.* **930**, L17 (2022), arXiv:2311.09484 [astro-ph.HE].

[10] K. Hioki and K.-I. Maeda, Measurement of the Kerr spin parameter by observation of a compact object's shadow, *Phys. Rev. D* **80**, 024042 (2009), arXiv:0904.3575 [astro-ph.HE].

[11] D. Psaltis *et al.* (Event Horizon Telescope), Gravitational Test Beyond the First Post-Newtonian Order with the Shadow of the M87 Black Hole, *Phys. Rev. Lett.* **125**, 141104 (2020), arXiv:2010.01055 [gr-qc].

[12] J. M. Bardeen, Timelike and null geodesics in the Kerr metric., in *Black Holes (Les Astres Occlus)* (1973) pp. 215–239.

[13] J. P. Luminet, Image of a spherical black hole with thin accretion disk, *Astron. Astrophys.* **75**, 228 (1979).

[14] S. E. Gralla, D. E. Holz, and R. M. Wald, Black hole shadows, photon rings, and lensing rings, *Phys. Rev. D* **100**, 024018 (2019), arXiv:1906.00873 [astro-ph.HE].

[15] M. D. Johnson *et al.*, Universal interferometric signatures of a black hole's photon ring, *sciadv* **6**, eaaz1310 (2020), arXiv:1907.04329 [astro-ph.IM].

[16] S. E. Gralla and A. Lupsasca, Lensing by Kerr black holes, *Phys. Rev. D* **101**, 044031 (2020), arXiv:1910.12873 [gr-qc].

[17] S. E. Gralla and A. Lupsasca, Observable shape of black hole photon rings, *Phys. Rev. D* **102**, 124003 (2020), arXiv:2007.10336 [gr-qc].

[18] H. Paugnat, A. Lupsasca, F. H. Vincent, and M. Wielgus, Photon ring test of the Kerr hypothesis: Variation in the ring shape, *aap* **668**, A11 (2022), arXiv:2206.02781 [astro-ph.HE].

[19] A. Cárdenas-Avendaño and A. Lupsasca, Prediction for the interferometric shape of the first black hole photon ring, *Phys. Rev. D* **108**, 064043 (2023), arXiv:2305.12956 [gr-qc].

[20] D. C. M. Palumbo, G. N. Wong, A. A. Chael, and M. D. Johnson, Demonstrating Photon Ring Existence with Single-baseline Polarimetry, *Astrophys. J. Lett.* **952**, L31 (2023), arXiv:2307.05293 [astro-ph.HE].

[21] K. Chatterjee, P. Kocherlakota, Z. Younsi, and R. Narayan, Energy Extraction from Spinning Stringy Black Holes, *arXiv e-prints*, arXiv:2310.20040 (2023), arXiv:2310.20040 [gr-qc].

[22] K. Chatterjee, Z. Younsi, P. Kocherlakota, and R. Narayan, On the Universality of Energy Extraction from Black Hole Spacetimes, *arXiv e-prints*, arXiv:2310.20043 (2023), arXiv:2310.20043 [gr-qc].

[23] M. D. Johnson *et al.*, Key Science Goals for the Next-Generation Event Horizon Telescope, *Galaxies* **11**, 61 (2023).

[24] M. D. Johnson *et al.*, The Black Hole Explorer: motivation and vision, *Proc. SPIE Int. Soc. Opt. Eng.* **13092**, 130922D (2024), arXiv:2406.12917 [astro-ph.IM].

[25] P. Galison, M. D. Johnson, A. Lupsasca, T. Gravely, and R. Berens, The Black Hole Explorer: using the photon ring to visualize spacetime around the black hole, *Proc. SPIE Int. Soc. Opt. Eng.* **13092**, 130926R (2024), arXiv:2406.11671 [gr-qc].

[26] T. Kawashima, Y. Tsunetoe, K. Ohsuga, M. Kino, Y. Mizuno,

K. Moriyama, H. Saida, K. Akiyama, K. Hada, and K. Niinuma, Black hole spacetime and properties of accretion flows and jets probed by Black Hole Explorer: science cases proposed by BHEX Japan team, *Proc. SPIE Int. Soc. Opt. Eng.* **13092**, 130926X (2024), arXiv:2406.09995 [astro-ph.HE].

[27] A. Lupsasca, A. Cárdenas-Avendaño, D. C. M. Palumbo, M. D. Johnson, S. E. Gralla, D. P. Marrone, P. Galison, P. Tiede, and L. Keeble, The Black Hole Explorer: photon ring science, detection, and shape measurement, *Proc. SPIE Int. Soc. Opt. Eng.* **13092**, 130926Q (2024), arXiv:2406.09498 [gr-qc].

[28] K. Akiyama *et al.*, The Japanese vision for the Black Hole Explorer mission, *Proc. SPIE Int. Soc. Opt. Eng.* **13092**, 130922E (2024), arXiv:2406.09516 [astro-ph.IM].

[29] K. Akiyama *et al.* (Event Horizon Telescope), First M87 Event Horizon Telescope Results. VI. The Shadow and Mass of the Central Black Hole, *Astrophys. J. Lett.* **875**, L6 (2019), arXiv:1906.11243 [astro-ph.GA].

[30] P. Kocherlakota *et al.* (Event Horizon Telescope), Constraints on black-hole charges with the 2017 EHT observations of M87*, *Phys. Rev. D* **103**, 104047 (2021), arXiv:2105.09343 [gr-qc].

[31] R. Kumar Walia, S. G. Ghosh, and S. D. Maharaj, Testing Rotating Regular Metrics with EHT Results of Sgr A*, *Astrophys. J.* **939**, 77 (2022), arXiv:2207.00078 [gr-qc].

[32] S. Vagnozzi *et al.*, Horizon-scale tests of gravity theories and fundamental physics from the Event Horizon Telescope image of Sagittarius A, *Class. Quant. Grav.* **40**, 165007 (2023), arXiv:2205.07787 [gr-qc].

[33] R. Kumar, A. Kumar, and S. G. Ghosh, Testing Rotating Regular Metrics as Candidates for Astrophysical Black Holes, *Astrophys. J.* **896**, 89 (2020), arXiv:2006.09869 [gr-qc].

[34] K. Glampedakis and G. Pappas, Is a black hole shadow a reliable test of the no-hair theorem?, *Phys. Rev. D* **107**, 064001 (2023), arXiv:2302.06140 [gr-qc].

[35] R. Kumar and S. G. Ghosh, Black Hole Parameter Estimation from Its Shadow, *Astrophys. J.* **892**, 78 (2020), arXiv:1811.01260 [gr-qc].

[36] N. Tsukamoto, Z. Li, and C. Bambi, Constraining the spin and the deformation parameters from the black hole shadow, *JCAP* **06**, 043, arXiv:1403.0371 [gr-qc].

[37] S. E. Gralla, Measuring the shape of a black hole photon ring, *Phys. Rev. D* **102**, 044017 (2020), arXiv:2005.03856 [astro-ph.HE].

[38] F. H. Vincent, S. E. Gralla, A. Lupsasca, and M. Wielgus, Images and photon ring signatures of thick disks around black holes, *aap* **667**, A170 (2022), arXiv:2206.12066 [astro-ph.HE].

[39] P. Kocherlakota, L. Rezzolla, R. Roy, and M. Wielgus, Prospects for future experimental tests of gravity with black hole imaging: Spherical symmetry, *Phys. Rev. D* **109**, 064064 (2024), arXiv:2307.16841 [gr-qc].

[40] P. Kocherlakota, L. Rezzolla, R. Roy, and M. Wielgus, Hotspots and photon rings in spherically-symmetric spacetimes, *mnras* **10.1093/mnras/stae1321** (2024), arXiv:2403.08862 [astro-ph.HE].

[41] S. Hadar, M. D. Johnson, A. Lupsasca, and G. N. Wong, Photon ring autocorrelations, *Phys. Rev. D* **103**, 104038 (2021), arXiv:2010.03683 [gr-qc].

[42] S. Hadar, D. Kapec, A. Lupsasca, and A. Strominger, Holography of the photon ring, *Class. Quant. Grav.* **39**, 215001 (2022), arXiv:2205.05064 [gr-qc].

[43] E. Himwich, M. D. Johnson, A. Lupsasca, and A. Strominger, Universal polarimetric signatures of the black hole photon ring, *Phys. Rev. D* **101**, 084020 (2020), arXiv:2001.08750 [gr-qc].

[44] H. Jia, E. Quataert, A. Lupsasca, and G. N. Wong, Photon ring interferometric signatures beyond the universal regime, *Phys. Rev. D* **110**, 083044 (2024), arXiv:2405.08804 [astro-ph.HE].

[45] S. Staelens, D. R. Mayerson, F. Bacchini, B. Ripperda, and L. Küchler, Black hole photon rings beyond general relativity, *Phys. Rev. D* **107**, 124026 (2023), arXiv:2303.02111 [gr-qc].

[46] P. Kocherlakota, L. Rezzolla, R. Roy, and M. Wielgus, Prospects for future experimental tests of gravity with black hole imaging: Spherical symmetry, *Phys. Rev. D* **109**, 064064 (2024), arXiv:2307.16841 [gr-qc].

[47] M. Wielgus, Photon rings of spherically symmetric black holes and robust tests of non-Kerr metrics, *Phys. Rev. D* **104**, 124058 (2021), arXiv:2109.10840 [gr-qc].

[48] L. F. D. da Silva, F. S. N. Lobo, G. J. Olmo, and D. Rubiera-Garcia, Photon rings as tests for alternative spherically symmetric geometries with thin accretion disks, *Phys. Rev. D* **108**, 084055 (2023), arXiv:2307.06778 [gr-qc].

[49] K. Salehi, R. Kumar, D. Chang, and P. Kocherlakota (2024), *in prep.*

[50] T. Johannsen, Regular Black Hole Metric with Three Constants of Motion, *Phys. Rev. D* **88**, 044002 (2013), arXiv:1501.02809 [gr-qc].

[51] K. Salehi, A. Broderick, and B. Georgiev, Photon Rings and Shadow Size for General Integrable Spacetimes, (2023), arXiv:2311.01495 [gr-qc].

[52] E. T. Newman, R. Couch, K. Chinnapared, A. Exton, A. Prakash, and R. Torrence, Metric of a Rotating, Charged Mass, *J. Math. Phys.* **6**, 918 (1965).

[53] A. Sen, Rotating charged black hole solution in heterotic string theory, *Phys. Rev. Lett.* **69**, 1006 (1992), arXiv:hep-th/9204046.

[54] C. Bambi and L. Modesto, Rotating regular black holes, *Phys. Lett. B* **721**, 329 (2013), arXiv:1302.6075 [gr-qc].

[55] D. Kapec and A. Lupsasca, Particle motion near high-spin black holes, *cqg* **37**, 015006 (2020), arXiv:1905.11406 [hep-th].

[56] K. Gebhardt, J. Adams, D. Richstone, T. R. Lauer, S. M. Faber, K. Güttekin, J. Murphy, and S. Tremaine, The Black Hole Mass in M87 from Gemini/NIFS Adaptive Optics Observations, *Astrophys. J.* **729**, 119 (2011), arXiv:1101.1954 [astro-ph.CO].

[57] GRAVITY Collaboration *et al.*, Detection of orbital motions near the last stable circular orbit of the massive black hole SgrA*, *aap* **618**, L10 (2018), arXiv:1810.12641 [astro-ph.GA].

[58] R. C. Walker and others, The Structure and Dynamics of the Subparsec Jet in M87 Based on 50 VLBA Observations over 17 Years at 43 GHz, *Astrophys. J.* **855**, 128 (2018), arXiv:1802.06166 [astro-ph.HE].

[59] R. P. Breton, V. M. Kaspi, M. Kramer, M. A. McLaughlin, M. Lyutikov, S. M. Ransom, I. H. Stairs, R. D. Ferdman, F. Camilo, and A. Possenti, Relativistic Spin Precession in the Double Pulsar, *Science* **321**, 104 (2008), arXiv:0807.2644 [astro-ph].